MRS Advances (2025) 10:2500–2506
https://doi.org/10.1557/s43580-025-01353-1

ORIGINAL PAPER

The first principles and experimental study of equilibrium and non-equilibrium low-temperature phases of $Nb_{50}Ru_{50}$ alloy

Duduzile Nkomo[1,2] · **Roelf Mostert**[2] · **Maje Phasha**[1]

Received: 22 January 2025 / Accepted: 24 July 2025 / Published online: 31 July 2025

Abstract

The equilibrium and non-equilibrium low-temperature phases of $Nb_{50}Ru_{50}$ alloy have been investigated using ab initio calculations (thermodynamic, elastic, and electronic properties) in conjunction with experimental microstructural and phase analyses. Low-temperature phases in $Nb_{50}Ru_{50}$ alloy originate from the transformation of tetragonal $L1_0$ phase at 750 °C, which potentially makes it useful for designing high-temperature shape memory alloys. Current results showed that the monoclinic phase *P2m* is the most energetically stable under equilibrium conditions, and this is complemented by the absence of negative frequencies in the phonon dispersion curves. However, negative frequencies were observed on the orthorhombic phase *Cmmm*, indicating that it is a metastable martensite phase. Therefore, two low-temperature phases of $Nb_{50}Ru_{50}$ have been determined, namely *P2m* and *Cmmm*. This forms the basis for further designing of the alloy with superior shape memory properties since *P2m* is softer and exhibits lower symmetry compared to the brittle $L1_0$ phase.

Introduction

The equiatomic niobium-ruthenium ($Nb_{50}Ru_{50}$) alloy is considered a potential HTSMA because of the transformation that occurs from the high-temperature ordered cubic structure (B2) to the tetragonal structure ($L1_0$) during cooling at 1100 °C. This transformation has shown shape memory properties; however, the shape recovery was considered poor with only 4% recovery strain compared to the ultimate recovery strain of about 10% observed in Ti-Ni SMA [1, 2]. This is attributed to the formation of the brittle $L1_0$ phase. Therefore, this triggered the current study, which focuses on the second transformation of $L1_0$ to a low-temperature phase around 750 °C. The identification of low-temperature phase will assist in determining whether or not the second transformation results in formation of phases that promotes shape memory properties, thus adding into the versatility of $Nb_{50}Ru_{50}$ alloy for applications such as turbomachinery and engine aircraft applications where high damping capacity, actuation, and high strength are a requirement [3–6].

The structure of a low-temperature phase remains a topic of interest because of the debate about its symmetry [7, 8]. Orthorhombic (Ortho) structure with *Cmmm* symmetry has been identified as a low-temperature phase [8, 9]. Other structures with *Pmma* and *Pmna* symmetries have been predicted [10]. On the other hand, the monoclinic (MCL) phase has been identified experimentally as the low-temperature phase [7, 11, 12]. Previously, researchers have reported different variants of the MCL phase using theoretical studies, where electronic properties of *P21m* [10, 13, 14] and *P2m* [14] were investigated. From these studies, the *P21m* appeared to be the most stable. However, the MCL phase with *P2m* symmetry was experimentally observed at room temperature [12].

Therefore, in an attempt to contribute toward resolving the above discrepancy, this paper aims to study the low-temperature phases of $Nb_{50}Ru_{50}$ alloy with the aid of first-principles calculations. Additionally, new possible structures of $Nb_{50}Ru_{50}$ are theoretically designed and evaluated for stability. The phonon dispersions and elastic and electronic properties of possible orthorhombic and monoclinic structures were predicted to elucidate the symmetry of the low-temperature phase. Phonon dispersions have been previously used to study the vibrational properties of alloys to predict the stability of phases, i.e., the presence of soft modes or negative frequencies implies that that particular structure

✉ Duduzile Nkomo
dudunk@mintek.co.za

[1] Advanced Materials Division, Mintek, 200 Malibongwe Drive, Randburg 2125, South Africa

[2] Department of Materials Science and Metallurgical Engineering, University of Pretoria, Hatfield, Pretoria 0028, South Africa

is not stable at 0 K and is likely to undergo further phase transformation [8, 14]. The elasticity data and the density of state calculations are normally used to obtain information about the mechanical stability and electronic properties of each structure [13–15].

Furthermore, experimental microstructural evolution and phase analysis were performed using a light microscope and X-ray diffraction techniques, respectively. Measurements were conducted at room temperature on furnace-cooled (FC) and water-quenched (WQ) samples to determine which low-temperature structures occur under equilibrium and non-equilibrium conditions. The distinction of the two is important in designing SMAs.

Computational method

The density functional theory (DFT)-based Cambridge Serial Total Energy Package (CASTEP) code was used to perform all calculations within the Materials Studio software package, version 2020 [16]. Robust Vanderbilt ultrasoft pseudopotentials [17] were used to describe the ion–electron interaction within the generalized gradient approximation (GGA) [18] of Perdew-Burke-Ernzerhof (PBE) [19]. All ground-state structures were optimized using the Broyden-Fletcher-Goldfarb-Shanno (BFGS) minimization scheme. The convergence criterion was set to less than 0.00001 eV/atom, with maximum residual forces of 0.03 eV/Å, the maximum residual bulk stress of 0.05 GPa, and the maximum atomic displacement of 0.001 Å. The crystal structures of the phases considered were built as shown in Fig. 1. The B2 (*Pm3m*) and $L1_0$ (*P4mmm)* structures were calculated using k-points of 16 × 16 × 16 and 19 × 19 × 13, respectively. Monoclinic structures were *P2m*, *P21m*, and *C2m*, for which the 8 × 18 × 13, 11 × 12 × 18 ,and 11 × 11 × 6 k-points were used. Orthorhombic structures were *Amm2*, *Cmmm,* and *Pmm2*, and the k-points of 18 × 18 × 16, 11 × 11 × 17 ,and 18 × 16 × 18 were used to perform calculations. The energy cutoff point of 700 eV was enough to converge all the systems studied. A small strain of 0.004 was used to calculate elastic constants. Lattice dynamic properties were set to a cutoff radius of 3.5 Å, utilizing the finite displacement supercell method within the code [20].

Experimental method

High-purity Nb and Ru compacted metal powders were melted using an arc-melting ultrasonic atomiser under a stringent vacuum and argon gas atmosphere. The ingots were rotated and re-heated six times to ensure homogeneous heating of the sample and to promote the proper mixing of the elements. Samples were solution-treated at 1200 °C for 4 h to eliminate any compositional gradient from dendritic solidification. One sample was slow-cooled in the furnace, while another was quenched in ice water. The microstructure was characterized using the DSX 500 OLYMPIC optical microscope on samples polished down to OP-U colloidal silica suspension with a grain size of 0.25 µm and etched with the Ru-based alloy etchant solution. Phase constituents were measured using the X-ray diffractometer (XRD) with radiation source of Cu kα1 tube operated at 45 kV and 40 mA. The 2θ angle scan range was measured from 5 to 100° at a step size of 0.01°.

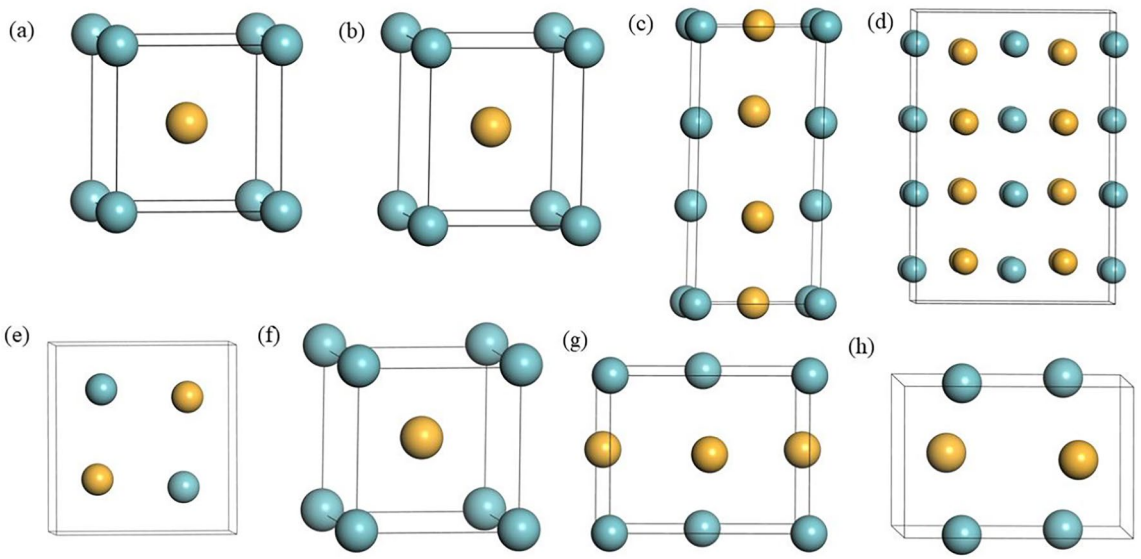

Fig. 1 Structures of $Nb_{50}Ru_{50}$: **a** B2 *Pm3m*, **b** $L1_0$ *P4mmm*; MCL: **c** *P2m*, **d** *C2m*, **e** *P21m*; and Ortho: **f** *Pmm2*, **g** *Amm2*, and **h** *Cmmm*

Results and discussions

Structural, thermodynamic, and elastic properties

Table 1 shows the calculated lattice parameters, heats of formation, and the elastic constants for the considered $Nb_{50}Ru_{50}$ structures. The lattice parameters of the B2 and $L1_0$ structures are consistent with theoretical and experimental literature values. The *P2m* and *Cmmm* lattice parameters agree well with the previously reported experimental values [8].

Equation (1) was used to calculate heats of formation (H_f) for all structures.

$$H_f = E_{\text{Total}} - \sum_i x_i E_i \tag{1}$$

where E_{Total} is the total energy of the compound, and E_i is the calculated total energies of the element *i* and x_i is the concentration of element *i* in the compound in their respective ground-state structures.

The monoclinic *P2m* structure is the most stable as indicated by the most negative value. The most thermodynamically favored orthorhombic structure is *Cmmm*, agreeing with the previous experimental data [8].

Furthermore, Table 1 shows the calculated elastic constants for the structures considered. The cubic B2 lattice consists of three independent constants: C_{11}, C_{12}, and

Table 1 Theoretical and literature lattice parameters, H_f, and elastic constants of $Nb_{50}Ru_{50}$ crystals

Lattice parameters (Å)				Thermodynamic stability
Symmetry	a	b	c	H_f (eV/atom)
Pm3m	3.170			− 0.1676
	3.179 [14]$^{\text{ab-initio}}$			− 0.182 [9]$^{\text{Exp}}$
	3.176 [8]$^{\text{Exp}}$			− 0.163 [21]$^{\text{ab-initio}}$
P4mmm	3.059	3.419		− 0.1959
	3.065	3.422 [14]$^{\text{ab-initio}}$		
	3.062	3.431 [22]$^{\text{ab-initio}}$		
	3.106	3.307 [8]$^{\text{Exp}}$		
P2m	4.942	3.076	4.545	− 0.2366
	4.850	3.014	4.357 [8]$^{\text{Exp}}$	
	4.745	3.026	4.482 [13]$^{\text{ab-initio}}$	
P21m	4.700	4.485	3.029	− 0.1961
	4.745	4.482	3.026 [13]$^{\text{ab-initio}}$	
C2m	4.582	3.084	4.527	− 0.2331
Pmm2	3.053	3.418	3.054	− 0.1928
Amm2	3.417	4.319	4.319	− 0.1929
Cmmm	3.041	3.396	3.084	− 0.2168
	3.014	3.430	3.081 [8]$^{\text{Exp}}$	

Calculated elastic constants (GPa)

C_{ij}	*Pm3m*	*P4mmm*	*P2m*	*P21m*	*C2m*	*Pmm2*	*Amm2*	*Cmmm*
C_{11}	125	351	333	296	324	304	339	311
C_{12}	287	146	149	196	175	171	182	196
C_{44}	69	58	58	65	75	42	58	45
C_{33}		305	334	357	336	314	344	362
C_{66}		56	59	− 373	65	42	42	19
C_{13}		173	201	157	197	193	209	172
C_{22}			370	325	354	316	301	354
C_{55}			78	21	59	52	42	18
C_{23}			179	176	158	177	216	168
C_{15}			− 5	10	10			
C_{25}			12	4	− 9			
C_{35}			− 1	7	11			
C_{46}			− 22	− 2	22			

$C_{44,}$ and the stability criteria are defined by $C_{11}-C_{12}>0$, $C_{44}>0$, and $C_{11}+2C_{12}>0$. There are six independent constants for the $L1_0$ crystal denoted as: C_{11}, C_{12}, C_{13}, C_{33}, C_{44} and C_{66} from which the mechanical stability criteria are as follows: $C_{11}>|C_{12}|$, $C_{33}>0$, $C_{44}>0$, $C_{66}>0$, $(C_{11}+C_{33}-2C_{13})>0$ and $(2C_{11}+C_{33}-2C_{12}+4_{13})>0$ [23]. For the orthorhombic crystal, the mechanical stability is determined by $(C_{11}+C_{22}-2C_{12})>0$, $(C_{11}+C_{33}-2C_{13})>0$, $(C_{22}+C_{33}-2C_{23})>0$ and $[C_{11}+C_{22}+C_{33}+2(C_{12}+C_{13}+C_{23})]>0$, while for the monoclinic crystal, the mechanical stability criteria are such that $C_{11}>0$, $C_{22}>0$, $C_{33}>0$, $C_{44}>0$, $C_{55}>0$, $C_{66}>0$, $C_{44}C_{66}-2C_{46}>0$, $C_{11}+C_{22}+C_{33}+2(C_{12}+C_{13}+C_{23})>0$, $C_{22}+C_{33}-2C_{23}>0$ [24]. The cubic B2 phase is not mechanically stable, while all other structures show stability. The *P2m* is the most mechanically stable of MCL structures, and *Cmmm* is the most stable of the orthorhombic structures.

Electronic and lattice dynamic properties

The calculated total electronic density of states (tDOS) for the considered structures of $Nb_{50}Ru_{50}$ alloy are shown if Fig. 2a. The tDOS has been used to predict the electronic properties of $Nb_{50}Ru_{50}$ structures by studying the behavior of energy states near the Fermi level. When the pseudogap is situated within the deep valley near the Fermi level ($E-E_f=0$), the structure is considered most stable, whereas the structure will be least stable when the Fermi level cuts the shoulder or the peak. Therefore, the *P2m* structure is the most stable of the $Nb_{50}Ru_{50}$ alloy.

Also shown in Fig. 2b–i are the lattice vibrational properties for all structures. The lattice vibrations for the B2 structure showed negative frequencies along the X-R, R-M, G-M, and G-R symmetry directions of the Brillouin zone (BZ). This indicates that the B2 phase is indeed an unstable structure at 0 K and thus readily undergoes martensitic transformation at high temperatures.

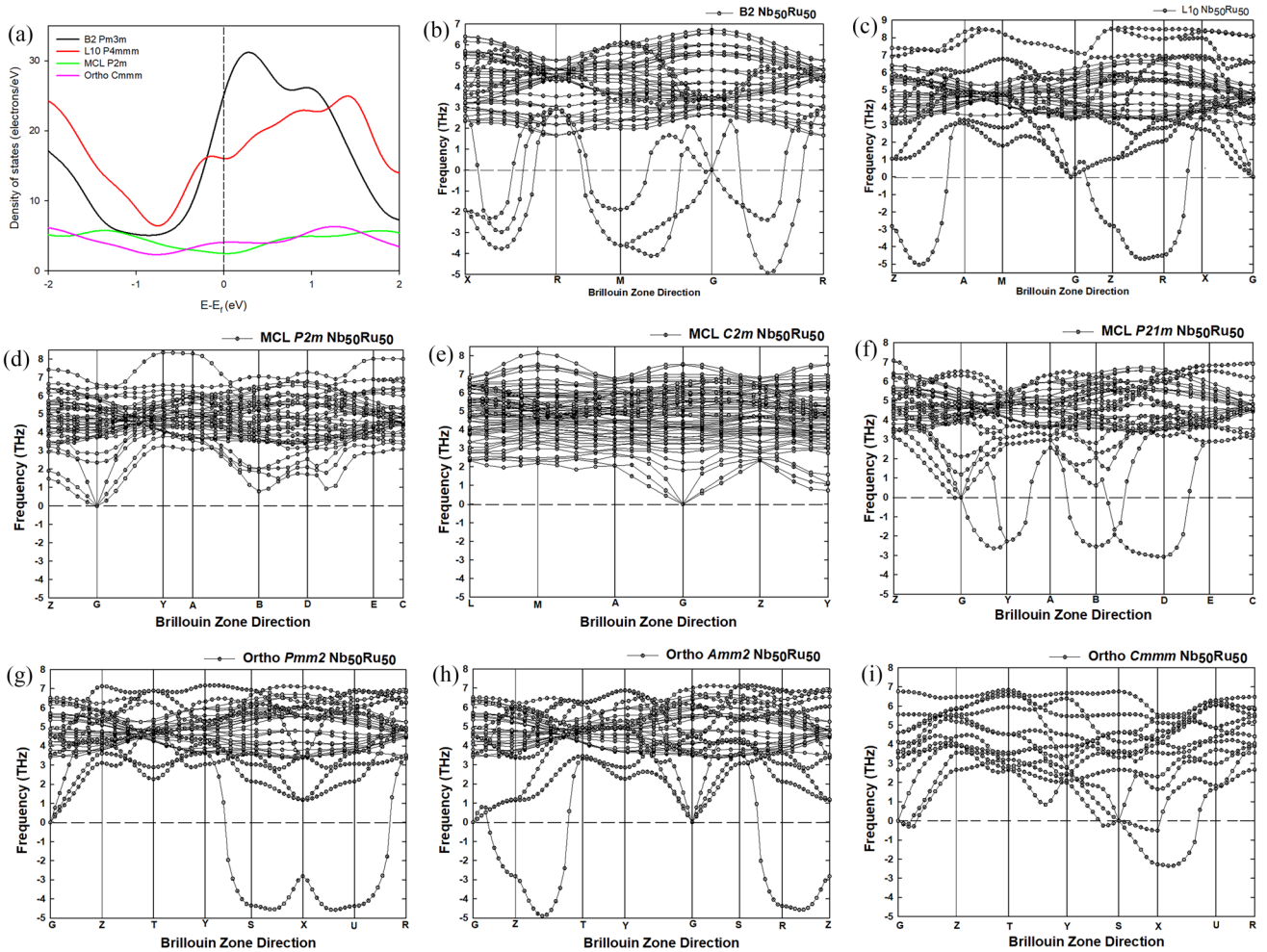

Fig. 2 **a** Total density of states (tDOS) of B2, $L1_0$, MCL (*P2m*), Ortho (*Cmmm*), and phonon dispersion curves of: **b** B2, **c** $L1_0$, **d–f** MCL: **d** *P2m*, **e** *C2m*, **f** *P21m*, and **g–i** Ortho: **g** *Pmm2*, **h** *Amm2* and **i** *Cmmm*

The phonon dispersions of the $L1_0$ phase also display negative frequencies along the symmetry axis Z-A, G-Z, Z-R, and R-X. These indicate vibration of atoms along the [110], [001], and [010] directions of the $L1_0$ lattice. The vibrations depict slight distortion along [001], predicting the formation of *P4mm* tetragonal structure. The orthorhombic structures with *Pmm2* and *Amm2* symmetry are likely to form from atomic vibrations on the $L1_0$ lattice along the [010] and [110] directions as shown by negative frequencies along the Z-R and R-X axis. In the case of $L1_0$, the presence of negative frequencies indicates that it is unstable; hence, it has been found to participate in the shape memory aspect of the $Nb_{50}Ru_{50}$ alloy [1].

Moreover, the absence of negative frequencies on the monoclinic structures *P2m* and *C2m* is indicative of stability. Based on the calculated heats of formation, this indicates that *P2m* is the ground-4state structure, while the negative frequencies on orthorhombic structures are indicative of metastability. Further investigation of whether or not the *P2m* or *Cmmm* low-temperature phases of $Nb_{50}Ru_{50}$ alloy exhibit shape memory properties is beyond the scope of this paper, but this will form part of future work.

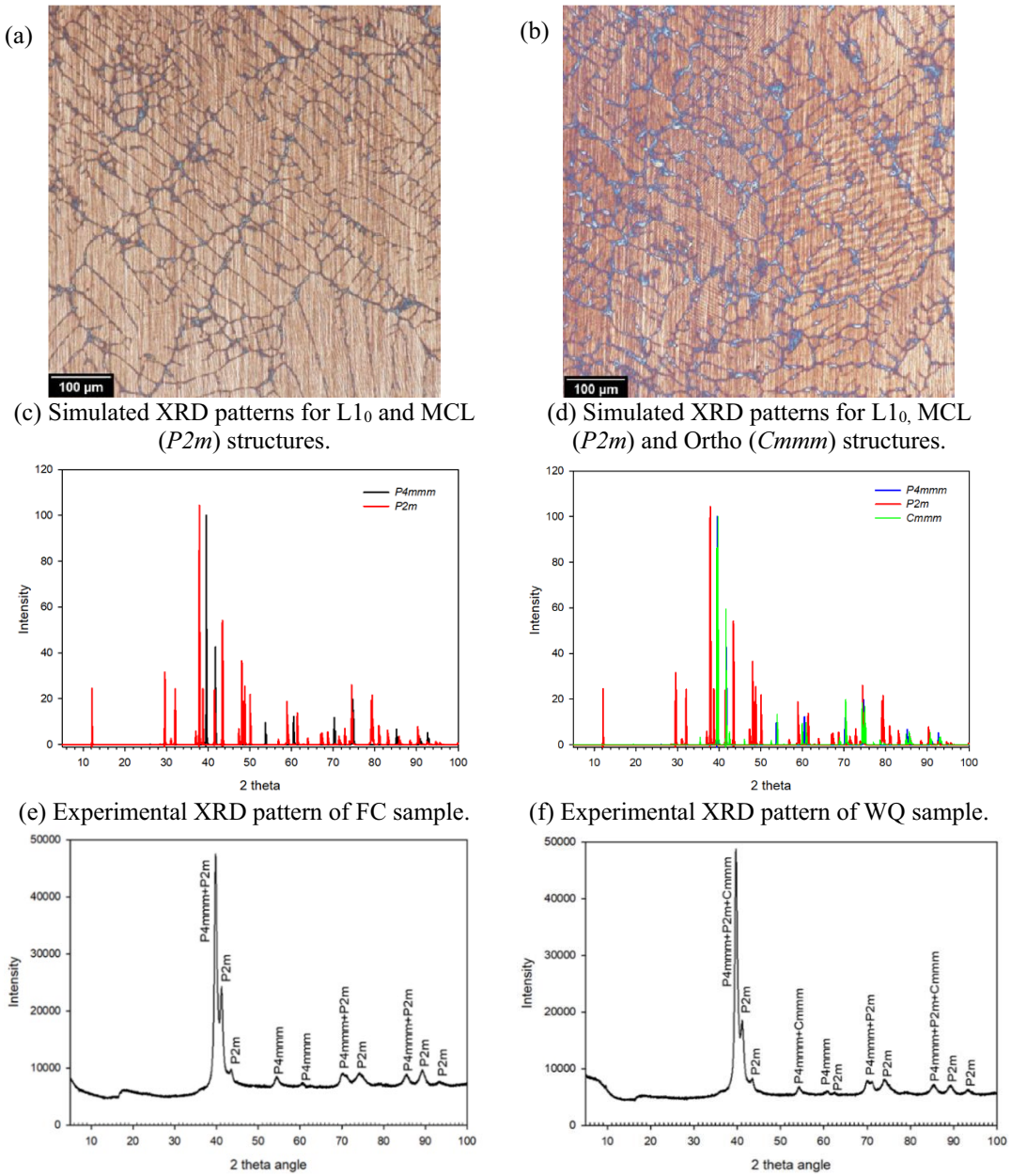

Fig. 3 Microstructure: **a** FC and **b** WQ samples, simulated XRD patterns: **c** FC and **d** WQ samples, experimental XRD: **e** FC and **f** WQ samples

Microstructure and phase analyses

Figure 3 shows the microstructure and the simulated and experimental XRD patterns of furnace-cooled (FC) and water-quenched (WQ) samples. Fine martensitic plates are observed on the FC sample, while the large martensitic plates are introduced on the quenched sample. The much larger, thick plates on the quenched sample are of the magnitude 5–10 µm. These plates seem to form independently from the original $L1_0$ phase during quenching, while the finer martensitic plates belong to the MCL phase, which forms within the fine plates of the $L1_0$ phase [11]. However, this needs to be further confirmed using an analytical instrument capable of much higher magnification, such as high-resolution TEM. To perform a first qualitative assignment of the experimentally obtained peaks, the XRD patterns were plotted alongside simulated patterns obtained from the Reflex code embedded within the Materials Studio package. The corresponding patterns suggest that the slow-cooled sample could consist mostly of $L1_0$ and MCL (*P2m*) phases, while the quenched sample shows a possible presence of an orthorhombic (*Cmmm*) phase in addition to equilibrium phases. A more quantitative X-ray analysis is necessary to confirm this hypothesis.

Conclusion

This study explored possible low-temperature structures of $Nb_{50}Ru_{50}$ alloy using ab initio calculations. The calculated heats of formation and elastic constants showed that the *P2m* monoclinic structure is the most thermodynamically and mechanically stable. Furthermore, the tDOS indicated that *P2m* is the most stable compared to B2, $L1_0$, monoclinic, and orthorhombic structures. The phonon dispersions indicated that *P2m* is indeed the ground-state structure of $Nb_{50}Ru_{50}$, while the orthorhombic structure *Cmmm* is the likely structure to be obtained under non-equilibrium conditions due to the presence of negative frequencies. Microstructural and XRD analysis showed the presence of fine martensitic plates, which were supported by XRD to be associated with the presence of both the $L1_0$ and the MCL phases on the slow-cooled sample. The water-quenched sample showed the introduction of thicker martensitic plates, which were presumably formed independently of the original $L1_0$ plates and assigned to the *Cmmm* structure. This study has successfully determined the ground-state and non-equilibrium low-temperature phases of $Nb_{50}Ru_{50}$ alloy. The viability of these structures in the design of $Nb_{50}Ru_{50}$ alloy with improved shape memory properties will be considered in future investigations.

Acknowledgments This work is published with the permission of Mintek. The authors would like to thank the Advanced Metals Initiative (AMI) of the Department of Science and Innovation (DSI), as well as the National Research Foundation (NRF) South Africa—JSPS [GRANT No: 148782] for financial support. The gratitude is also extended to the Centre for High-Performance Computing (CHPC) in Cape Town for allowing us to carry out the calculations using their remote computing resources.

Author contributions All authors contributed to the study conception and design. Material preparation, data collection, and analysis were performed by Duduzile Nkomo, Roelf Mostert, and Maje Phasha. The first draft of the manuscript was written by Duduzile Nkomo and all authors commented on previous versions of the manuscript. All authors read and approved the final manuscript. Conceptualization: Duduzile Nkomo, Roelf Mostert, and Maje Phasha; Methodology: Duduzile Nkomo, Roelf Mostert, and Maje Phasha; Formal analysis and investigation: Duduzile Nkomo and Maje Phasha; Writing—original draft preparation: Duduzile Nkomo; Writing—review and editing: Duduzile Nkomo, Roelf Mostert, and Maje Phasha; Funding acquisition: Roelf Mostert and Maje Phasha; Resources: Duduzile Nkomo, Roelf Mostert, and Maje Phasha; Supervision: Roelf Mostert and Maje Phasha.

Funding Open access funding provided by Mintek. Open access funding was provided by Mintek.

Data availability Data can be made available upon request from the corresponding author.

Declarations

Competing interests The authors declare no conflict of interest.

References

1. R.W. Fonda, H.N. Jones, R.A. Vandermeer, Scr. Mater. **39**, 8 (1998)
2. J.M. Jani, M. Leary, A. Subic, M.A. Gibson, Mater. Des. **56**, 443 (2014)
3. K.P. Duffy, S.A. Padula II., D.A. Scheiman, Behav. Mech. Multifunct. Compos. Mater. **14**, 6929 (2008)
4. D.J. Hartl, D.C. Lagoudas, Proc. Inst. Mech. Eng. G J. Aerosp. Eng. **221**, 4 (2007)
5. D.A. Exarchos, P.T. Dalla, I.K. Tragazikis, K.G. Dassios, N.E. Zafeiropoulos, M.M. Karabela, C. De Crescenzo, D. Karatza, D. Musmarra, S. Chianese, T.E. Matikas, Materials **11**, 5 (2018)
6. G.S. Firstov, J. Van Humbeeck, Y.N. Koval, Mater. Sci. Eng. A **378**, 1–2 (2004)

7. B.K. Das, M.A. Schmerling, D.S. Lieberman, Metall. Trans. **1**, 61801 (1970)
8. S.M. Shapiro, G. Xu, G. Gu, J. Gardner, R.W. Fonda, Phys. Rev. B Condens. Matter Mater. Phys. **73**, 21 (2006)
9. C.L. Tan, W. Cai, X.H. Tian, Chin. Phys. B **19**, 3 (2010)
10. P. Shao, L. Ding, D. Luo, J. Cai, C. Lu, J. Alloys Compd. **695**, 1 (2017)
11. P. Vermaut, A. Manzoni, A. Denquin, F. Prima, R.A. Portier, Mater Charact **142**, 109 (2018)
12. A.M. Manzoni, A. Denquin, P. Vermaut, F. Prima, I. Puente-Orench, C. Pauly, F. Mücklich, R.A. Portier, Acta Mater. **111**, 283 (2016)
13. A.A. Mousa, B.A. Hamad, J.M. Khalifeh, Eur. Phys. J. B. **72**, 4 (2009)
14. Z. Wu, O. Benafan, J.W. Lawson, Acta Mater. **276**, 120140 (2024)
15. C. Tan, W. Cai, X. Tian, Scr. Mater. **56**, 7 (2007)
16. J. Pokluda, M. Černý, M. Šob, Y. Umeno, Prog. Mater. Sci. **73**, 223 (2015)
17. D. Vanderbilt, Phys. Rev. B **41**, 7892 (1990)
18. J.P. Perdew, Y. Wang, Phys. Rev. Lett. **77**, 1 (1992)
19. J.P. Perdew, K. Burke, M. Ernzerhof, Phys. Rev. Lett. **77**, 18 (1996)
20. M.A. Hadi, S.R.G. Christopoulos, A. Chroneos, S.H. Naqib, A.K.M.A. Islam, Sci. Rep. **12**, 1 (2022)
21. M.Y. Benarchid, N. David, J.M. Fiorani, M. Vilasi, T. Benlaharche, Thermochim. Acta **482**, 1–2 (2009)
22. W. Chen, R. Yuan, F. Tan, W. Xu, Phys. Chem. Chem. Phys. **24**, 37 (2022)
23. G. Grimvall, B. Magyari-Köpe, E.N.M. Ozoliņ, K.A. Persson, Rev. Mod. Phys. **84**, 2 (2012)
24. J. Chang, X. Zhou, K. Liu, N. Ge, R. Soc, Open Sci. **5**, 7 (2018)